FRONTIERS OF PHYSICS

RESEARCH ARTICLE
Volume 17 / Issue 6 / 63509 / 2022

Computational exploration and screening of novel Janus MA_2Z_4 (M = Sc–Zn, Y–Ag, Hf–Au; A=Si, Ge; Z=N, P) monolayers and potential application as a photocatalyst

Weibin Zhang[1,†], Woochul Yang[3], Yingkai Liu[1], Zhiyong Liu[1], Fuchun Zhang[2,‡]

1 College of Physics and Electronics Information, Yunnan Key Laboratory of Opto-Electronic Information Technology, Key Laboratory of Advanced Technique & Preparation for Renewable Energy Materials-Ministry of Education, Yunnan Normal University, Kunming 650500, China
2 College of Physics and Electronic Information, Yan'an University, Yan'an 716000, China
3 Department of Physics, Dongguk University, Seoul 04620, Republic of Korea
Corresponding authors. E-mail: †220001@ynnu.edu.cn, ‡yadxzfc@yau.edu.cn
Received July 5, 2022; accepted August 3, 2022

ABSTRACT

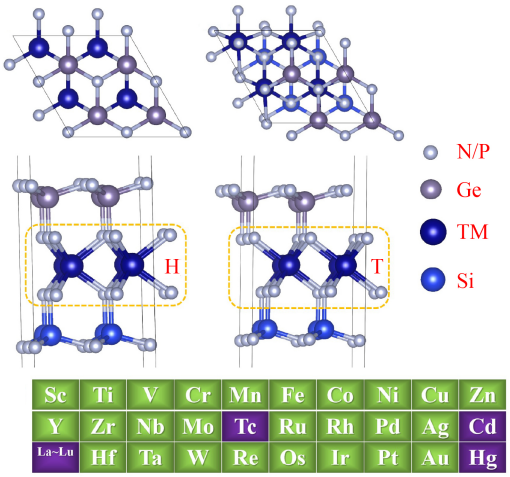

By high-throughput calculations, 13 thermally and environmentally stable Janus MA_2Z_4 monolayers were screened from 104 types of candidates. The 13 stable monolayers have very high charge carrier concentrations ($\times 10^{15}$ cm^{-2}), which are better than those of the well-known graphene and TaS_2. Because of their excellent conductivity, the 6 monolayers with band gaps less than 0.5 eV are identified as potential electrode materials for hydrogen evolution reaction applications. For potential applications as photoelectric or photocatalytic materials, bandgaps ($E_{g\text{-HSE}}$) higher than 0.5 eV remained, which resulted in 7 potential candidates. Based on optical absorption analysis in the visible-light range, H-$HfSiGeP_4$ and H-$MoSiGeP_4$ have higher absorption ability and optical conductivity, which is quite impressive for optoelectronic, solar cell device, and photocatalysis applications. Additionally, the transmittance coefficient of Janus MA_2Z_4 monolayers is approximately 70%–80% in the visible-light range, which implies that these monolayers show good light transmittance. For potential applications as photocatalysts, the redox potential and charge effective mass analysis indicate that H-$HfSiGeP_4$, H-$MoSiGeP_4$, T-$ScSiGeN_4$, and T-$ZrSiGeN_4$ are suitable photocatalysts for CO_2 reduction reactions. Using high-throughput identification, 13 types of new and stable Janus MA_2Z_4 monolayers were explored, and the basic properties and potential applications were investigated, which can reduce the time for experiments and provide basic data for the material genome initiative.

Keywords Janus MA_2Z_4, high-throughput identification, charge carrier concentration, electronic structure, optical properties

1 Introduction

Two-dimensional (2D) materials have attracted extensive attention because of their unique properties, including high specific surface, excellent stability, and low cost. Therefore, experimental and theoretical studies have been widely performed because of their potential applications in electronics and optoelectronics, field-effect

https://doi.org/10.1007/s11467-022-1199-5

transistors, catalysis, and energy storage [1]. Diverse types of 2D materials with good properties and diverse potential applications have been widely investigated, including phosphides [2], and g-C_3N_4 [3] transition-metal chalcogenides [4]. However, few 2D candidates have practical and industrialized applications, such as the hydrogen evolution reaction (HER), NO removal or CO_2 reduction. Therefore, it is urgent to explore new 2D materials or mechanisms by calculations and experimental efforts to satisfy the extending requirements of the applications.

In 2020, Ren *et al.* [5] first synthesized $MoSi_2N_4$ using a chemical vapor deposition method. This material exhibited semiconducting behavior (band gap ~1.94 eV), high strength (~66 GPa), and excellent environmental stability. Because of its excellent physical and chemical properties, the $MoSi_2N_4$ monolayer has attracted considerable attention. Li *et al.* [6] investigated the possibility of $MoSi_2N_4$ as both the cathode and anode of Zn–air batteries and revealed the mechanism of Zn storage. Ma *et al.* [7] investigated the adsorption behavior of environmental gas molecules on pristine and defective $MoSi_2N_4$ and indicated that this material could be applied as a highly sensitive and reusable gas sensor. Ye *et al.* [8] predicted the performances of double-gate metal oxide semiconductor field effect transistors (MOSFETs) based on monolayer $MoSi_2N_4$, and the results revealed that monolayer $MoSi_2N_4$ was a promising alternative for transistor channel materials in the post-silicon era. Optical analysis shows that the $MoSi_2N_4$ monolayer is a promising candidate as a photocatalyst for hydrogen evolution [9] and CO_2 reduction [10, 11].

Due to the aforementioned outstanding performance and various applications, many researchers have explored the family of 2D (2D) materials, including atom doping, adsorption, and atomic layer replacement, to develop new types of 2D materials [2, 12]. Two-dimensional Janus structures have attracted increasing attention because of the unique properties caused by their out-of-plane asymmetry. Janus structures have been successfully achieved in many 2D materials, such as Janus graphene [13], silicone [14], PtSSe [15], TiXY (X/Y = S, Se and Te) [16], VSSe [17, 18], SnSSe [19], TMDs [20, 21], and M_2XY (M = Ga, In; X/Y = S, Se, Te) [22]. Therefore, the Janus structure of $MoSi_2N_4$ can also be achieved, and some researchers have reported the stability and potential applications of the Janus structure of the $MoSi_2N_4$ family, such as $MoSiGeN_4$ and $WSiGeN_4$ monolayers. Guo *et al.* [23] predicted that Janus $MSiGeN_4$ (M = Mo and W) monolayers had very good dynamic, mechanical and thermodynamic stability and were indirect band-gap semiconductors. Yu *et al.* [24] reported Janus $MoSiGeN_4$ and $WSiGeN_4$ structures with excellent stabilities that can be applied as photocatalysts. Binh *et al.* [25] constructed ultrathin graphene and Janus $MoGeSiN_4$ van der Waals heterostructures and investigated the Schottky barriers and interfacial electronic properties. However, there is no systematically exploration and screening of Janus MA_2Z_4 monolayers.

Therefore, the systematic exploration and screening of stable Janus MA_2Z_4 (M = Sc-Zn, Y–Ag, Hf–Au; A = Si, Ge; Z = N, P) monolayer are urgent. This work applied high-throughput calculations to screen 104 types of Janus MA_2Z_4 monolayers and explored 13 stale candidates. The charge carrier concentrations, band gap, density of states, and optical properties were investigated. The potential applications as photocatalysts were also investigated. Using high-throughput calculations, 13 types of new and stable Janus MA_2Z_4 monolayers were explored, which can reduce the time for the experiment and provide basic data for the material genome initiative.

2 Computational details

The *Vienna ab initio* simulation (VASP) package [26] based on the first-principle method is applied in this calculation. The GGA (generalized gradient approximation)-PBE (Perdew–Burke–Ernzerhof) [27] exchange-correlation function was applied for geometry optimization, while the electronic and optical properties were calculated by Heyd–Scuseria–Ernzerhof (HSE06) method [28]. The convergence thresholds in energy and force on each atom were 2.0×10^{-6} eV and 0.002 eV/Å, respectively. The energy cutoff was set to 450 eV for the plane-wave basis. Brouin zone integration was performed on a 3 × 3 × 1 k-point grid, and the rationality was verified by calculations with a higher cutoff energy and a k-point grid.

The interactions between photons and electrons can be described in terms of time-dependent perturbations of the ground electronic state based on quantum mechanics. The electron transitions between different states are caused by photon absorption or emission. The optical spectra can be accepted by the joint density of states in the conduction and valence bands. The imaginary part $[\varepsilon_2(\omega)]$ can be written as follows [29, 30]:

$$\varepsilon_2(q\to O_{\widehat{u}}, h\omega) = \frac{2\pi e^2}{\Omega\varepsilon_0}\sum\nolimits_{k,v,c}|\langle\psi_{\boldsymbol{k}}^c|\boldsymbol{u}\cdot r|\psi_{\boldsymbol{k}}^v\rangle|^2\delta(E_{\boldsymbol{k}}^c - E_{\boldsymbol{k}}^v - E), \quad (1)$$

where u is the vector defining the incident electric field's polarization, and k is the reciprocal lattice vector. The superscripts c and v denote the conduction band (CB) and valence band (VB), respectively, and ω is the incident photon frequency. Using Kramers–Kroning relations, the real part (ε_1) of the dielectric function can be obtained from ε_2. Then, $\varepsilon_1(\omega)$ and $\varepsilon_2(\omega)$ can be applied to obtain the optical spectra as the absorption coefficient $(\alpha(\omega))$, reflectivity $R(\omega)$, and refractivity index $[n(\omega)]$:

$$\alpha(\omega) = \left[\sqrt{\varepsilon_1{}^2(\omega) + \varepsilon_2{}^2(\omega)} - \varepsilon_1(\omega)\right]^{1/2}, \quad (2)$$

$$n(\omega) = \left[\sqrt{\varepsilon_1{}^2(\omega) + \varepsilon_2{}^2(\omega)} + \varepsilon_1(\omega)\right]^{1/2} \Big/ \sqrt{2}, \quad (3)$$

$$R(\omega) = \left|\frac{\sqrt{\varepsilon_1(\omega) + i\varepsilon_2(\omega)} - 1}{\sqrt{\varepsilon_1(\omega) + i\varepsilon_2(\omega)} + 1}\right|^2. \quad (4)$$

3 Results and discussion

3.1 Structures and dynamic stability

Figure 1 demonstrates the element compositions and chemical structures for the Janus MA_2Z_4 monolayers, where M represents 3*d*, 4*d* and 5*d* transition-metal (*TM*) elements, A denotes Si and Ge elements, and Z is for N and P elements (M = Sc-Zn, Y–Ag, Hf–Au; A = Si, Ge; Z = N, P). The Janus MA_2Z_4 materials have a sandwich structure: the inner part is the transition-metal dichalcogenide-like MZ_2 monolayer (including H and T phases), which is covered by two hexagonal AZ monolayers. Therefore, there are two proposed structures of H- and T-phases for every Janus MA_2Z_4 monolayer, denoted as Janus H(T)-MA_2Z_4 in Fig. 1. Considering the radioactive, toxic and unstable nature, the transition metals Tc, Cd, Hg and La-Lu were not considered in this study. Considering the stochastic combination of element compositions (26 × 1 × 2) and chemical structures (2), 104 types of Janus MA_2Z_4 monolayers are prepared for the following calculations.

The thermal and environmental stabilities are important to the practical application of Janus MA_2Z_4. The phonon dispersions were calculated to evaluate the stability of the 104 candidates. There are 13 candidates with no imaginary frequency in the first Brillouin zone, which verifies their dynamical stability with no soft modes. The phonon dispersions of H-$MoSiGeN_4$ and T-$ScSiGeN_4$ are shown in Figs. 2(a, c) as the representative, and the phonon dispersions of the residual 11 candidates are shown in Figs. S1 and S2.

Then, the thermal stability of the 13 selected Janus MA_2Z_4 was evaluated by AIMD (ab initio molecular dynamics) simulations. During the AIMD simulations, the supercells were set to be 2 × 2, and the temperature was 300 K with a Nose thermostat. The simulation time was 5 ps, and the step time was 1 fs. As shown in Figs. 2(b, d), the temperature and energy fluctuate around the equilibrium values without any sudden changes for H-$MoSiGeN_4$ and T-$ScSiGeN_4$. The residual 11 candidates show similar phenomena. Therefore, the 13 selected Janus MA_2Z_4 monolayers can maintain their structural integrity at room temperature, which indicates their good thermal stability.

3.2 Electronic properties of Janus MA_2Z_4 monolayers

The electronic properties were determined to screen the Janus MA_2Z_4 monolayers for different applications. The PBE and HSE06 band structure calculations were performed for the 13 monolayers. Janus MA_2Z_4 monolayers with HSE06 band gaps ($E_{g\text{-HSE}}$) lying outside the 0.5–3.26 eV were left out from this subset, which resulted in 7 potential photocatalysts (H-$ZnSiGeN_4$, H-$MoSiGeN_4$, H-$MoSiGeP_4$, H-$HfSiGeP_4$, H-$WSiGeN_4$, T-$ScSiGeN_4$, T-$ZrSiGeN_4$). The band structures of the 7 candidates are shown in Fig. 3, and the band gap values are tabulated in Table 1. This criterion was chosen to

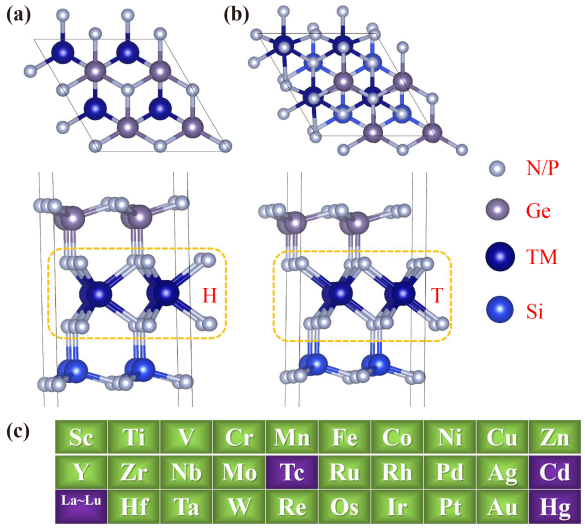

Fig. 1 Top and side views of the **(a)** H- and **(b)** T-phase structures of the Janus MA_2Z_4 monolayer. **(c)** Periodic table of the 3d, 4d and 5d transition metals (*TM*) in the work.

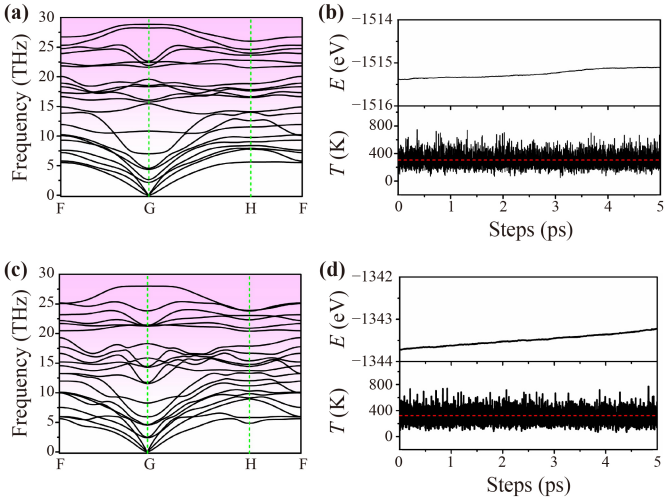

Fig. 2 **(a)** Phonon band dispersion, **(b)** total energy and variation in temperature of H-$MoSiGeN_4$; **(c)** phonon band dispersion, **(d)** total energy and variation in temperature of T-$ScSiGeN_4$.

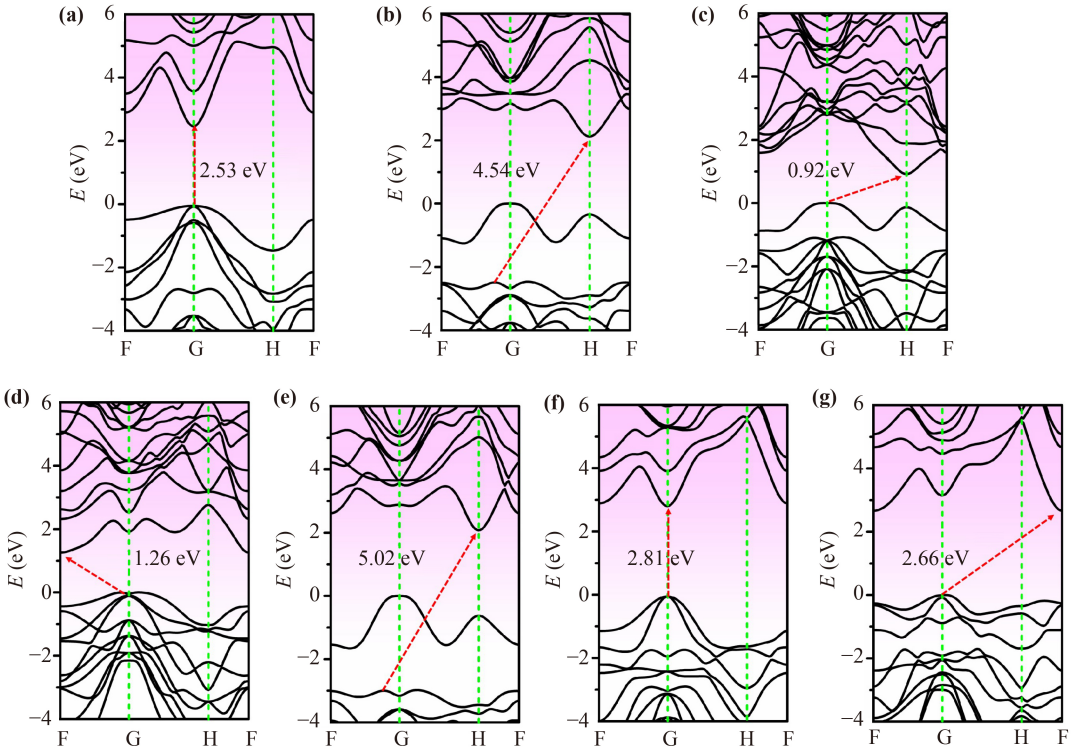

Fig. 3 Band structures of **(a)** H-$ZnSiGeN_4$, **(b)** H-$MoSiGeN_4$, **(c)** H-$MoSiGeP_4$, **(d)** H-$HfSiGeP_4$, **(e)** H-$WSiGeN_4$, **(f)** T-$ScSiGeN_4$, and **(g)** T-$ZrSiGeN_4$. The Fermi level was set to 0.

Table 1 Band gap (eV), work function (Φ, eV), valence band maximum (*VBM*), conduction band edge (*CBM*), electron/hole effective mass (m_e^*/m_h^*), static dielectric constant ε_r (0), and carrier concentration (n) of the 7 selected Janus MA_2Z_4 monolayers.

	$E_{g\text{-PBE}}$	$E_{g\text{-HSE}}$	Φ	*VBM*	*CBM*	m_e^*	m_h^*	*D*	ε_1 (0)	n (10^{15}cm^{-2})
H-$ZnSiGeN_4$	2.1	2.53	6.35	2.76	0.23	0.11	1.55	14.73	4.79	1.11
H-$MoSiGeN_4$	1.27	4.54	5.58	4.86	0.32	0.19	4.83	26.06	2.98	0.21
H-$MoSiGeP_4$	0.28	0.92	5.26	1.02	0.10	0.15	1.26	8.54	4.90	0.63
H-$HfSiGeP_4$	0.62	1.26	6.07	1.17	–0.09	0.19	0.73	3.87	4.38	1.81
H-$WSiGeN_4$	1.27	5.02	5.23	5.46	0.44	0.13	1.80	14.41	2.89	0.31
T-$ScSiGeN_4$	2.1	2.81	6.89	2.66	–0.15	0.12	0.39	3.23	3.35	0.33
T-$ZrSiGeN_4$	1.41	2.66	6.23	2.65	–0.01	0.26	0.55	2.12	2.53	2.33

ensure that the selected Janus MA_2Z_4 was optically active for photoelectric, photovoltaic or photocatalysis applications.

The partial density of states (PDOSs) and total density of states (TDOS) of H-$MoSiGeN_4$ and T-$ScSiGeN_4$ were investigated. Figure 4(a) shows the PDOSs and TDOS of H-$MoSiGeN_4$. E_{VB} (valence band edge) is mainly contributed by Mo 4*d* and N 2*p* orbital hybridization. E_{CB} (conduction band edge) is mainly contributed by the Mo 4*d* orbital. For the T-$ScSiGeN_4$ case in Fig. 4(b), E_{VB} is mainly contributed by the Sc 3*d* and N 2*p* orbital hybridization. E_{CB} is mainly contributed by the Sc 3*d* orbital. The DOS for the residual 7 candidate are shown in Fig. S3. These materials have similar phenomena: E_{VB} is mainly contributed by *TM d* and N/P *p* orbital hybridization, while E_{CB} is mainly contributed by the *d* orbitals of *TM*s.

The charge carrier concentration character is one of the most important factors to evaluate potential applications of semiconductors. Herein, based on the DOS data, the charge carrier concentrations were calculated and analyzed. Fermi–Dirac distribution can be approximated as a step function at very low temperatures. Therefore, the carrier densities (n) can be obtained by integrating the electronic TDOS around the Fermi level (E_F). To verify the reliability of the calculations, we also calculated the carrier density of graphene and TaS_2. Based on this method, the calculated carrier concentration of graphene is 3.15×10^{13} cm^{-2}, which is quite comparable with other reports [(2–5) $\times 10^{13}$ cm^{-2}] [31, 32]. For the TaS_2 case, the calculated carrier concentration is 0.85×10^{15} cm^{-2}, which is very close to a previous report (1.01 ×

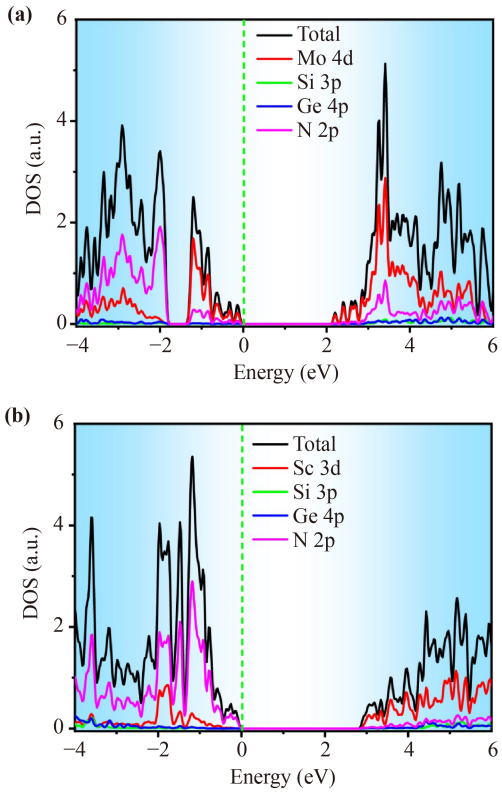

Fig. 4 Density of state of **(a)** H-$MoSiGeN_4$ and **(b)** T-$ScSiGeN_4$. The Fermi level was set to 0.

10^{15} cm^{-2}) [33]. Therefore, our calculation method is reasonable and can be applied in the following investigations. Based on this method, the carrier densities of stable Janus MA_2Z_4 monolayers are listed in Table 1 and Table 2. The carrier concentrations of the 13 stable monolayers are on the order of 10^{15} cm^{-2}, which are better than those of the widely applied materials graphene and TaS_2. The highest case is T-$ZrSiGeN_4$, which is 2.33×10^{15} cm^{-2}. Therefore, these stable Janus MA_2Z_4 monolayers can be applied as potential electrodes or photoelectric devices because of their high charge carrier density. Additionally, they are good potential photocatalysts because the high carrier density can facilitate carrier transfer and is favorable for contact between the photo-induced charge and the molecules on the surface.

Table 2 Band gap (eV), work function (Φ, eV), and carrier concentration (n) of the 6 Janus MA_2Z_4 monolayers with band gap values below 0.5 eV.

	$E_{g\text{-PBE}}$	$E_{g\text{-HSE}}$	Φ	n (10^{15} cm^{-2})
H-$CrSiGeP_4$	0	0	4.268	1.09
H-$ZnSiGeP_4$	0	0.1	5.195	1.06
T-$ScSiGeP_4$	0	0.17	5.387	0.38
T-$ZnSiGeP_4$	0	0.43	4.941	0.38
T-$YSiGeP_4$	0	0	5.292	0.81
T-$PdSiGeP_4$	0	0.36	4.792	0.20

The band gaps ($E_{g\text{-PBE}}$ and $E_{g\text{-HSE}}$) below 0.5 eV (H-$CrSiGeP_4$, H-$ZnSiGeP_4$, T-$ScSiGeP_4$, T-$ZnSiGeP_4$, T-$YSiGeP_4$, T-$PdSiGeP_4$) are tabulated in Table 2. Because of the band gaps below 0.5 eV and high conductivities (carrier concentrations in magnitude of 10^{15} cm^{-2}), all 6 candidates are excellent conductive materials, which are helpful for electron transfer to accelerate the proton–electron recombination during the hydrogen evolution reaction (HER). Therefore, the 6 candidates are identified as suitable electrode materials for HER applications because the excited electrons in the materials can cross this low band gap and induce metallic properties at room temperature.

Because of the high charge carrier concentrations, the Janus MA_2Z_4 monolayers are proposed to be promising photo-electric materials applications such as solar cells, light-emitting diodes, and field emitters. For these applications, the work function is an important factor to evaluate the conversion efficiency and device performance. The work function (Φ) is formally defined as [34]

$$\Phi = I - E_F, \tag{5}$$

where I is the potential energy at an infinite distance from the system, and E_F is the Fermi level. Table 1 and Table 2 show the calculated work functions of the stable Janus MA_2Z_4 monolayers. It is the surface dipole formed by the interaction between atoms that should be responsible for the observed variation in the work function.

3.3 Optical properties of the Janus MA_2Z_4 monolayers

Optical property investigations can provide basic data to evaluate potential applications as photoelectric or photocatalytic materials. The dielectric constant is the synopsis of these optical properties. The static (when $\omega = 0$) dielectric constant $\varepsilon_1(0)$ was calculated and is tabulated in Table 1. Previous reports suggest that materials with a lower band gap show higher static dielectric constants [35]. In Table 1, the band gap decreased with increasing static dielectric constant. Materials with a higher static dielectric constant show a lower charge carrier recombination rate, which facilitates solar cell performance and photocatalysis. Therefore, materials with higher static dielectric constants, such as H-$ZnSiGeN_4$ H-$MoSiGeP_4$ and H-$HfSiGeP_4$, will be more suitable for solar cells and photocatalysis applications.

Figures 5 (a) and (b) depict the energy-dependent parameters of the imaginary part of the dielectric constants $\varepsilon_2(\omega)$ for Janus MA_2Z_4 monolayers ($E_{g\text{-HSE}}$ higher than 0.5 eV). The imaginary parts of the dielectric functions $\varepsilon_2(\omega)$ of H-$MoSiGeN_4$ and T-$ScSiGeN_4$ are analyzed as representations. For H-$MoSiGeN_4$ [the black line in Fig. 5(a)], the main peak is located at 8.94 eV, which corresponds to one of the intrinsic plasma frequencies. The peak originates from an electronic transition from the edge of the N $2p$ level in the valence

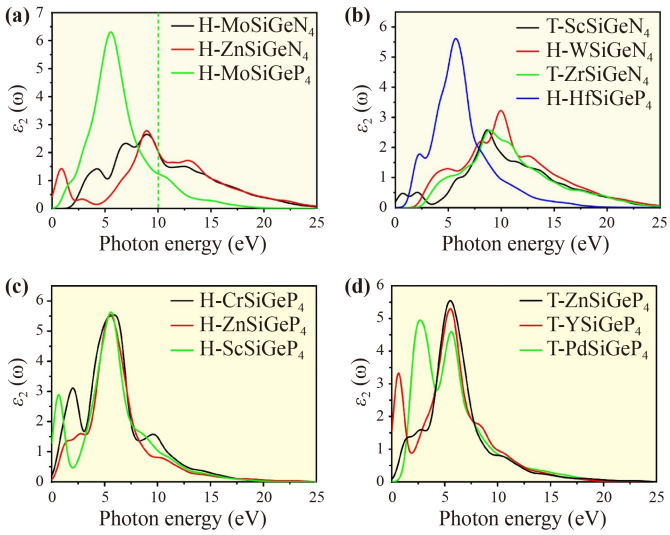

Fig. 5 **(a, b)** are imaginary part of the dielectric functions of the Janus MA_2Z_4 monolayers ($E_{g\text{-}HSE}$ higher than 0.5 eV); **(c, d)** are imaginary part of the dielectric functions of the Janus MA_2Z_4 monolayers ($E_{g\text{-}HSE}$ lower than 0.5 eV).

band at approximately –6.80 eV to the edge of the Mo 4*d* level in the conduction band at approximately 2.20 eV [Fig. 4(a)]. The peak at 4.19 eV originates from electronic transitions from the edge of the N 2*p* level in the valence band at approximately –2.02 eV to the edge of the conduction band of Mo 4*d* states at approximately 2.21 eV. For T-ScSiGeN$_4$ [the black line in Fig. 5(b)], the main peak is located at 8.72 eV, which corresponds to one of the intrinsic plasma frequencies. The peak originates from an electronic transition from the edge of the N 2*p* level in the valence band at approximately –6.20 eV to the edge of the Sc 3*d* level in the conduction band at approximately 2.80 eV [Fig. 4(b)]. The peak at 2.10 eV is attributed to the intraband transitions from the edge of the Sc 3*d* level in the valence band at –1.96 eV to the edge of the N 2p states at 0 eV. The other Janus MA_2Z_4 monolayers are not analyzed in detail. However, the peaks are mainly contributed from the electron transition between N/P *p* orbitals and TM *d* orbitals.

Figures 5 (c, d) depict the energy-dependent parameters of the imaginary part of the dielectric constants $\varepsilon_2(\omega)$ for Janus MA_2Z_4 monolayers with $E_{g\text{-}HSE}$ less than 0.5 eV. The imaginary parts of the dielectric functions $\varepsilon_2(\omega)$ of H-CrSiGeP$_4$ and T-PdSiGeP$_4$ are analyzed as representations. For H-CrSiGeP$_4$ (the black line in Figure 5c), the main peak is located at 5.97 eV, which corresponds to one of the intrinsic plasma frequencies. For T-PdSiGeP$_4$ [the green line in Fig. 5(d)], the main peak is located at 2.72 eV, which corresponds to one of the intrinsic plasma frequencies. The peaks are mainly contributed from the electron transition between N/P *p* orbitals and TM *d* orbitals.

The optical properties of the material, such as its refractive index (n) or absorption coefficient (α), are critical for several display and optical applications. For example, in camera lenses for smartphones or optical components for augmented reality devices, glasses with varying refractive index of 1.2–2.5, are often preferred. For solar energy conversion applications, a higher absorption coefficient in the visible light range is preferred.

The photo-absorption range and coefficient are important factors to assess the potential applications in photovoltaic, photocatalysis or other optoelectronic applications. The main optical absorption peaks of the Janus MA_2Z_4 monolayers are in the ultraviolet region (Fig. 6). For $E_{g\text{-}HSE}$ higher than 0.5 eV cases [Figs. 6(a, b)], in the visible-light range, H-HfSiGeP$_4$ and H-MoSiGeP$_4$ have higher absorption abilities, which are potentially suitable for photocatalysis applications. For $E_{g\text{-}HSE}$ less than 0.5 eV cases [Figs. 6(c, d)], the main optical absorption peaks of the Janus MA_2Z_4 monolayers are in the ultraviolet region also. However, in the visible-light range, H-CrSiGeP$_4$ and T-PdSiGeP$_4$ have one additional absorption peak, indicating the two materials have higher photo absorption ability than the other cases.

Then, Fig. 7 shows the functions $n(\omega)$ (refractivity index), $R(\omega)$ (reflectivity), and $L(\omega)$ (energy loss) of the seven Janus MA_2Z_4 monolayers. The H-MoSiGeN$_4$ monolayer is analyzed as a representation [the black line in Fig. 7(a1)]. In the lower energy range (<5.00 eV), the reflectivity and refractivity are relatively low. The ~5.00–10.00 eV photon-energy range is characterized by stronger reflectivity, and the refractivity and refractivity spectra have similar tendencies. When the electrons traverse the material, there is some energy loss, which can be described with the energy-loss function. The highest peak is located at approximately 18.89 eV in

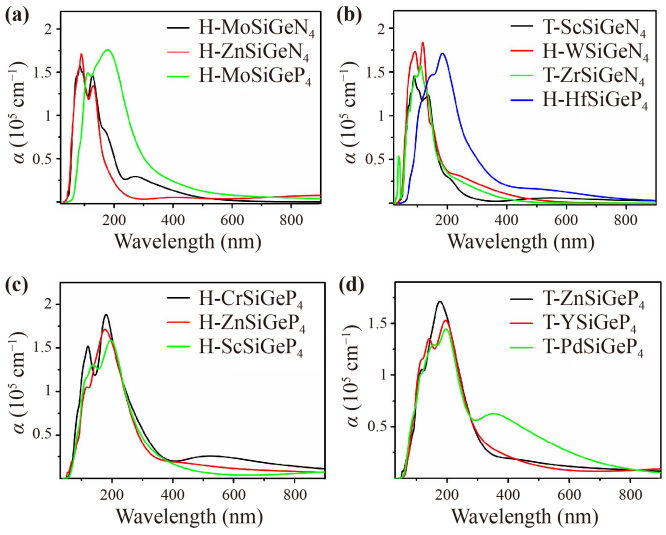

Fig. 6 **(a, b)** are optical absorption of the Janus MA_2Z_4 monolayers ($E_{g\text{-}HSE}$ higher than 0.5 eV); **(c, d)** are optical absorption for the Janus MA_2Z_4 monolayers ($E_{g\text{-}HSE}$ lower than 0.5 eV).

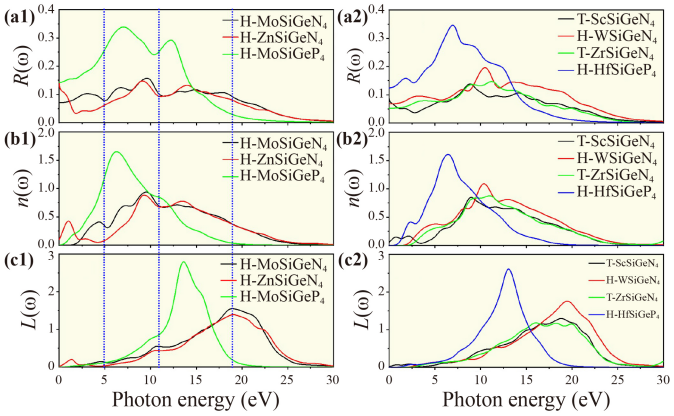

Fig. 7 **(a)** Reflectivity [$R(\omega)$], **(b)** refractivity index [$n(\omega)$], and **(c)** energy loss [$L(\omega)$] spectrum of the seven Janus MA_2Z_4 monolayers.

Fig. 7(c1), which is related to the existence of plasma oscillations. Additionally, the peaks of the energy-loss spectra are near the trailing edges of the reflection spectra. For the H-$MoSiGeN_4$ case, there are wave troughs at approximately 4.95 and 11.11 eV for $R(\omega)$, which correspond to the wave crest of $L(\omega)$. The other systems of Janus MA_2Z_4 monolayers have similar tendencies. H-$MoSiGeP_4$ and H-$HfSiGeP_4$ are in the ideal refractive index range and preferred for application as camera lenses.

The degree of electron transport in the substance can be described with the optical conductivity spectrum. In Fig. 8, the Janus MA_2Z_4 monolayers exhibit a significant optical conductivity under ultraviolet light. H-$HfSiGeP_4$, H-$MoSiGeP_4$, H-$CrSiGeP_4$, T-$PdSiGeP_4$ show better optical conductivity in visible light range, which indicates

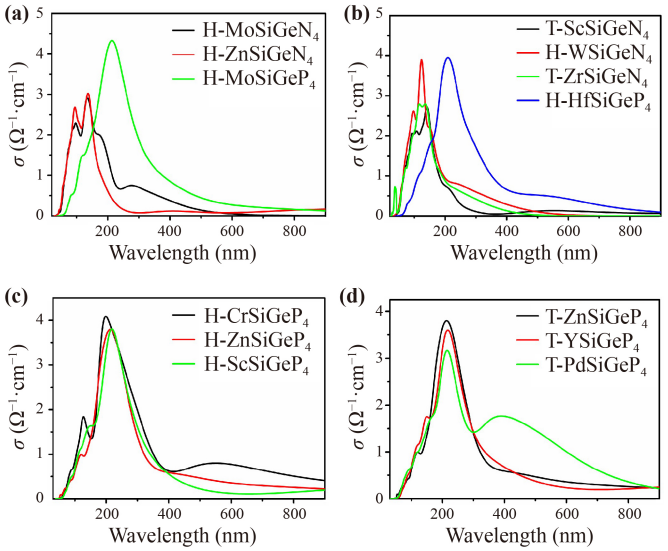

Fig. 8 **(a, b)** are optical conductivity for the Janus MA_2Z_4 monolayers ($E_{g\text{-}HSE}$ higher than 0.5 eV); **(c, d)** are optical conductivity for the Janus MA_2Z_4 monolayers ($E_{g\text{-}HSE}$ lower than 0.5 eV).

that the photo-induced charge carriers can quickly be transferred to the surface, which is quite impressive for optoelectronic, solar cell device, and photocatalysis applications.

Then, the transmittance spectra indicate the transmittance of the materials, which is also an important factor for the design of optical devices and can be calculated by the following formula [36]:

$$T = \frac{(1-R)^2 \exp(-\alpha d)}{1 - R^2 \exp(-2\alpha d)}, \tag{6}$$

where α is the absorption coefficient, R is the reflectivity, and d is the thickness of the material. The multiple reflections between front and back surfaces of the film are ignored. d is set to 50 nm in this work. As shown in Fig. 9, in the visible-light range, the transmittances of H-$HfSiGeP_4$ and H-$MoSiGeP_4$ are less than 70%, which implies that more photons are absorbed or reflected. However, the transmittance spectra are approximately 70%–80% in the visible-light range, which implies that the Janus MA_2Z_4 monolayers show good light transmittance.

3.4 Potential applications as photocatalysts

The relative effective masses of photo-induced charge carriers are important for photovoltaics or photocatalysis,

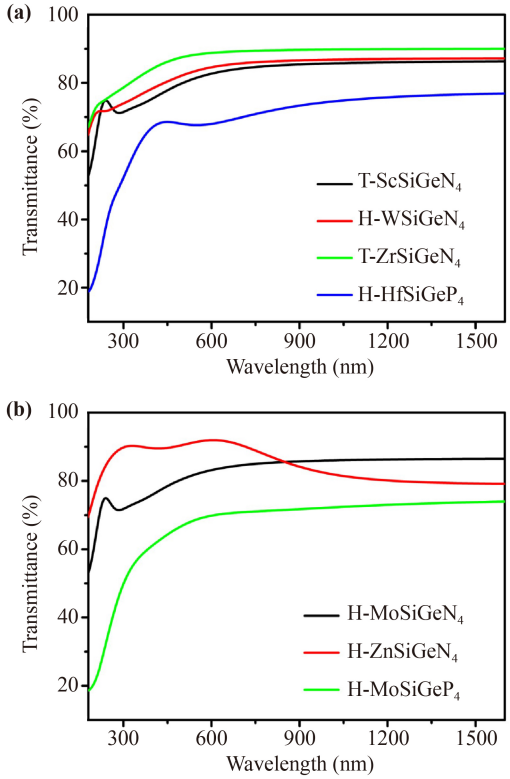

Fig. 9 **(a, b)** Transmittance spectra of Janus MA_2Z_4 monolayers.

which can determine the charge separation efficiency. Based on the electronic band structure results, the effective mass of electrons (e^-) and holes (h^+) of Janus MA_2Z_4 monolayers were calculated via parabolic fitting to the conduction band minimum (*CBM*) and valence band maximum (*VBM*), respectively. The effective masses of $e^-$and h^+ were calculated as follows:

$$m^* = \pm\frac{\hbar^2}{\mathrm{d}^2E/\mathrm{d}k^2}, \tag{7}$$

where m^* is the effective mass of the charge carrier, and $\mathrm{d}^2E/\mathrm{d}k^2$ is the coefficient of the second-order term in a quadratic fit of $E(k)$ curves for the band edge. The relative ratio (D) of the effective masses plays a significant role in photocatalysis and is evaluated as follows:

$$D = \frac{m_h^*}{m_e^*}. \tag{8}$$

By definition, the photogenerated e^-–h^+ pairs are more inclined to be separated when D is higher, and e^- and h^+ can migrate and enrich on the surface of materials.

The effective mass results of photoinduced e^-–h^+ of 7 selected Janus MA_2Z_4 monolayers and some reported materials are tabulated in Tables 1 and S1. The electron effective mass (m_e^*) of the selected Janus MA_2Z_4 monolayers is lighter than $Bi_4O_5Br_2$ [29], $BiVO_4$ [37], g-C_3N_4 [38], or TiO_2 [39], which are well-known photocatalysis or photovoltaic materials. Therefore, based on the charge effective mass analysis, the selected 7 Janus MA_2Z_4 monolayers have higher photocatalytic activity than the above three photocatalysts.

For photocatalysis applications, redox potential lines are a prerequisite for the catalytic reaction. For example, in photocatalytic NO removal or H_2O splitting, the *CBM* must be more negative than the redox potential of H^+/H_2 (0 V vs. NHE), while the *VBM* must be more positive than the redox potential of O_2/H_2O (1.23 V) [40, 41]. Therefore, it is important to calculate the redox potential and evaluate the potential applications of the materials.

Herein, the energy positions of the *VBM* and *CBM* of Janus MA_2Z_4 monolayers are calculated as follows [42]:

$$E_{VB} = X - E_e + 0.5E_g, \tag{9}$$

$$E_{CB} = E_{VB} - E_g. \tag{10}$$

X is the absolute electronegativity of the semiconductor, which is accepted by the geometric mean of the absolute electronegativity of the constituent atoms. With this method, the calculated X values of WO_3 and CdS are 6.59 and 5.18, respectively, which are almost the same as those in previous reports [43, 44] and verify that this method can be applied in future research. E_e is the energy of free electrons on the hydrogen scale (4.50 eV). E_g is accepted to have an HSE06 function. Table 1 shows the *VBM* and *CBM* of various Janus MA_2Z_4 monolayers calculated from Eqs. (9) and (10). Based on these judgment rules, H-$HfSiGeP_4$, H-$MoSiGeP_4$, T-$ScSiGeN_4$, T-$ScSiGeN_4$ and T-$ZrSiGeN_4$ are suitable for the CO_2 reduction reaction (CO_2RR) [45], as shown in Fig. 10.

Based on the redox potential analysis, another issue in the CO_2RR catalyst design is to obtain the energy-containing product (CH_4, CO, etc.), which is closely related to the activation energies (E_a) of radical reaction intermediates. Herein, we calculated the energy changes for all possible elementary hydrogenation steps of the CO_2RR on Janus MA_2Z_4 monolayers. Based on the redox potential analysis, T-$ScSiGeN_4$ and H-$HfSiGeP_4$ may have better photocatalytic performance, and the CO_2RR pathways were investigated, as shown in Fig. 11.

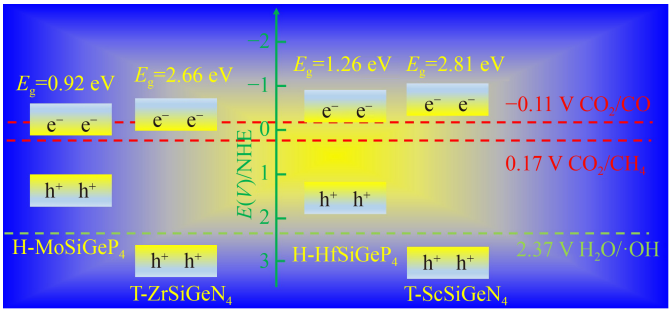

Fig. 10 Band alignments of the selected Janus MA_2Z_4 monolayers for the photocatalytic reduction of CO_2. The band edges are given with respect to the normal hydrogen electrode (NHE) potential (in volts).

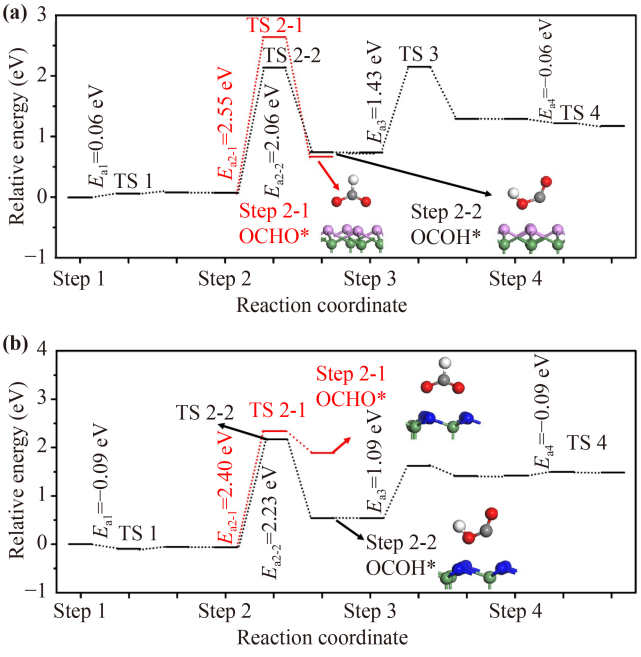

Fig. 11 Global reaction profiles for the CO_2RR on **(a)** H-$HfSiGeP_4$ and **(b)** T-$ScSiGeN_4$ (energy in eV).

The 1st step is CO_2 activation. The activation energies (E_{a1}) of H-$HfSiGeP_4$ and T-$ScSiGeN_4$ are 0.06 and –0.09 eV, respectively, which indicates that CO_2 can be easily activated. T-$ScSiGeN_4$ can automatically adsorb CO_2 because of the negative activation energy. Therefore, the first step can easily occur.

The 2nd hydrogenation (H^+/e^-) reactions are energetically prone to form OCOH* (Step 2-2) and energetically preferred than OCHO* (Step 2-1). Since OCOH* will always form CO* by releasing one H_2O molecule, the CO production can be the main product in CO_2 reduction by Janus MA_2Z_4.

Then, after the hydrogenation reaction, OCOH* will be further reduced to CO* with the release of one H_2O molecule. The activation energies (E_{a3}) of H-$HfSiGeP_4$ and T-$ScSiGeN_4$ are 1.43 and 1.09 eV, respectively. The final step is CO release. The activation energies (E_{a4}) of H-$HfSiGeP_4$ and T-$ScSiGeN_4$ are –0.06 and 0.09 eV, respectively, which implies that CO can be easily released on the surface. The reaction processes to reduce CO_2 to CO are listed below according to the abovementioned analysis.

Step 1: $CO_2(g) \rightarrow CO_2^*$,

Step 2-1: $CO_2^* + H^+ + e^- \rightarrow OCHO^*$,

Step 2-2: $CO_2^* + H^+ + e^- \rightarrow OCOH^*$,

Step 3: $OCOH^* + H^+ + e^- \rightarrow CO^* + H_2O \uparrow$,

Step 4: $CO^* \rightarrow CO \uparrow$.

Given the analysis above, four monolayers can accept the redox potential requirement for the CO_2RR: H-$MoSiGeP_4$, H-$HfSiGeP_4$, T-$ScSiGeN_4$, and T-$ZrSiGeN_4$. However, the photo absorption of H-$MoSiGeP_4$ and H-$HfSiGeP_4$ is the strongest in the visible-light range, and the relative ratio (D) of the electron/hole effective mass is larger in the four monolayers. Therefore, H-$MoSiGeP_4$ and H-$HfSiGeP_4$ are proposed as the best CO_2RR catalysts.

4 Conclusion

In summary, using high-throughput calculations, 104 types of Janus MA_2Z_4 materials were prepared in the initial space for screening and evaluation. The thermal and environmental stability investigations indicate that 13 candidates are stable. Because of their excellent conductivity, the 6 monolayers with band gaps below 0.5 eV were identified as potential electrode materials for hydrogen evolution reaction applications. For potential applications in photoelectric applications, Janus MA_2Z_4 monolayers with HSE06 band gaps ($E_{g\text{-}HSE}$) above 0.5 eV remained, which resulted in 7 potential candidates. Based on the *DOS* analysis, E_{VB} is mainly contributed by *TM d* and N/P *p* orbital hybridization, while E_{CB} is mainly contributed by the d orbitals of *TM*s. The carrier concentrations of the 13 stable monolayers are on the order of 10^{15} cm^{-2}, which are better than those of well-known graphene and TaS_2. The highest case is T-$ZrSiGeN_4$, which is 2.33×10^{15} cm^{-2}. Based on the optical absorption analysis, in the visible-light range, H-$HfSiGeP_4$ and H-$MoSiGeP_4$ have higher absorption ability and optical conductivity, which is quite impressive for optoelectronic, solar cell device, and photocatalysis applications. The transmittance spectra of the Janus MA_2Z_4 monolayers are approximately 70%–80% in the visible light range, which implies that these monolayers show good light transmittance. For potential applications as a CO_2RR photocatalyst, the redox potential and charge effective mass analysis indicate that H-$HfSiGeP_4$, H-$MoSiGeP_4$, T-$ScSiGeN_4$, and T-$ZrSiGeN_4$ are suitable for the CO_2RR. By high-throughput identification, 13 types of new and stable Janus MA_2Z_4 monolayers were explored, and the basic properties and potential applications were investigated, which can reduce the time for experiments and provide basic data for the material genome initiative.

Electronic supplementary material The supplementary material is available in the online version of this article at https://doi.org/10.1007/s11467-022-1199-5 and https://journal.hep.com.cn/fop/EN/pdf/10.1007/s11467-022-1199-5 and is accessible for authorized users.

CRediT authorship contribution statement Weibin Zhang: Data Curation, Investigation, Writing. Woochul Yang, Yingkai Liu & Zhiyong Liu: Review & Editing. Fuchun Zhang: Conceptualization, Methodology.

Declaration of competing interest The authors declare that they have no known competing financial interests or personal relationships that could have influenced the work reported in this paper.

Acknowledgements This research was supported by the National Natural Science Foundation of China (No. 52262042) and the Starting Funds for High-level Talents from Yunnan Normal University.

References

1. A. Bafekry, M. Faraji, D. M. Hoat, M. Shahrokhi, M. M. Fadlallah, F. Shojaei, S. A. H. Feghhi, M. Ghergherehchi, and D. Gogova, $MoSi_2N_4$ single-layer: A novel two-dimensional material with outstanding mechanical, thermal, electronic and optical properties, *J. Phys. D* 54(15), 155303 (2021)
2. Y. Xiao, C. Shen, and W. B. Zhang, Screening and prediction of metal-doped α-borophene monolayer for nitric oxide elimination, *Mater. Today Chem.* 25, 100958 (2022)
3. Y. Li, Z. Xia, Q. Yang, L. Wang, and Y. Xing, Review on g-C_3N_4-based S-scheme heterojunction photocatalysts, *J. Mater. Sci. Technol.* 125, 128 (2022)
4. H. Li, H. Li, Z. Wu, L. Zhu, C. Li, S. Lin, X. Zhu, and Y. Sun, Realization of high-purity 1T-MoS_2 by hydrothermal synthesis through synergistic effect of nitric acid and ethanol for supercapacitors, *J. Mater.*

Sci. Technol. 123, 34 (2022)
5. Y. L. Hong, Z. B. Liu, L. Wang, T. Y. Zhou, W. Ma, C. Xu, S. Feng, L. Chen, M. L. Chen, D. M. Sun, X. Q. Chen, H. M. Cheng, and W. C. Ren, Chemical vapor deposition of layered two-dimensional $MoSi_2N_4$ materials, *Science* 369(6504), 670 (2020)
6. X. M. Li, Z. Z. Lin, L. R. Cheng, and X. Chen, Layered $MoSi_2N_4$ as electrode material of Zn-air battery, *Phys. Status Solidi Rapid Res. Lett.* 16(5), 2200007 (2022)
7. C. Xiao, Z. Ma, R. Sa, Z. Cui, S. Gao, W. Du, X. Sun, and Q. Li, Adsorption behavior of environmental gas molecules on pristine and defective $MoSi_2N_4$: Possible application as highly sensitive and reusable gas sensors, *ACS Omega* 7(10), 8706 (2022)
8. B. Ye, X. Jiang, Y. Gu, G. Yang, Y. Liu, H. Zhao, X. Yang, C. Wei, X. Zhang, and N. Lu, Quantum transport of short-gate MOSFETs based on monolayer $MoSi_2N_4$, *Phys. Chem. Chem. Phys.* 24(11), 6616 (2022)
9. C. Xiao, R. Sa, Z. Cui, S. Gao, W. Du, X. Sun, X. Zhang, Q. Li, and Z. Ma, Enhancing the hydrogen evolution reaction by non-precious transition metal (Non-metal) atom doping in defective $MoSi_2N_4$ monolayer, *Appl. Surf. Sci.* 563, 150388 (2021)
10. A. Bafekry, M. Faraji, D. M. Hoat, M. Shahrokhi, M. M. Fadlallah, F. Shojaei, S. A. H. Feghhi, M. Ghergherehchi, and D. Gogova, $MoSi_2N_4$ single-layer: A novel two-dimensional material with outstanding mechanical, thermal, electronic and optical properties, *J. Phys. D* 54(15), 155303 (2021)
11. N. Mwankemwa, H. E. Wang, T. Zhu, Q. Fan, F. Zhang, and W. Zhang, First principles calculations investigation of optoelectronic properties and photocatalytic CO_2 reduction of $(MoSi_2N_4)_{5-n}/(MoSiGeN_4)_n$ in-plane heterostructures, *Results Phys.* 37, 105549 (2022)
12. T. Yang, J. Zhou, T. T. Song, L. Shen, Y. P. Feng, and M. Yang, High-throughput identification of exfoliable two-dimensional materials with active basal planes for hydrogen evolution, *ACS Energy Lett.* 5(7), 2313 (2020)
13. R. Singh and G. Bester, Hydrofluorinated graphene: Two-dimensional analog of polyvinylidene fluoride, *Phys. Rev. B* 84(15), 155427 (2011)
14. M. L. Sun, Q. Q. Ren, S. K. Wang, J. Yu, and W. C. Tang, Electronic properties of Janus silicene: New direct band gap semiconductors, *J. Phys. D* 49(44), 445305 (2016)
15. R. Peng, Y. Ma, B. Huang, and Y. Dai, Two-dimensional Janus PtSSe for photocatalytic water splitting under the visible or infrared light, *J. Mater. Chem. A* 7(2), 603 (2019)
16. A. Mogulkoc, Y. Mogulkoc, S. Jahangirov, and E. Durgun, Characterization and Stability of Janus TiXY (X/Y = S, Se, and Te) Monolayers, *J. Phys. Chem. C* 123(49), 29922 (2019)
17. L. X. Wang, Z. Lin, and Y. K. An, Tunable valley polarization, magnetic anisotropy and dipole moment for layered Janus 2H-VSSe with intrinsic room temperature ferromagnetism, *J. Alloys Compd.* 854, 157141 (2021)
18. C. M. Zhang, Y. H. Nie, S. Sanvito, and A. J. Du, First-principles prediction of a room-temperature ferromagnetic Janus VSSe monolayer with piezoelectricity, ferroelasticity, and large valley polarization, *Nano Lett.* 19(2), 1366 (2019)
19. S. D. Guo, X. S. Guo, R. Y. Han, and Y. Deng, Predicted Janus SnSSe monolayer: A comprehensive first-principles study, *Phys. Chem. Chem. Phys.* 21(44), 24620 (2019)
20. Y. C. Cheng, Z. Y. Zhu, M. Tahir, and U. Schwingenschlogl, Spin–orbit-induced spin splittings in polar transition metal dichalcogenide monolayers, *Europhys. Lett.* 102(5), 57001 (2013)
21. A. Y. Lu, H. Y. Zhu, J. Xiao, C. P. Chuu, Y. M. Han, M. H. Chiu, C. C. Cheng, C. W. Yang, K. H. Wei, Y. M. Yang, Y. Wang, D. Sokaras, D. Nordlund, P. D. Yang, D. A. Muller, M. Y. Chou, X. Zhang, and L. J. Li, Janus monolayers of transition metal dichalcogenides, *Nat. Nanotechnol.* 12(8), 744 (2017)
22. Y. Guo, S. Zhou, Y. Z. Bai, and J. J. Zhao, Enhanced piezoelectric effect in Janus group-III chalcogenide monolayers, *Appl. Phys. Lett.* 110(16), 163102 (2017)
23. S. D. Guo, W. Q. Mu, Y. T. Zhu, R. Y. Han, and W. C. Ren, Predicted septuple-atomic-layer Janus $MSiGeN_4$ (M = Mo and W) monolayers with Rashba spin splitting and high electron carrier mobilities, *J. Mater. Chem. C* 9(7), 2464 (2021)
24. Y. D. Yu, J. Zhou, Z. L. Guo, and Z. M. Sun, Novel two-dimensional Janus $MoSiGeN_4$ and $WSiGeN_4$ as highly efficient photocatalysts for spontaneous overall water splitting, *ACS Appl. Mater. Interfaces* 13(24), 28090 (2021)
25. N. T. T. Binh, C. Q. Nguyen, T. V. Vu, and C. V. Nguyen, Interfacial electronic properties and tunable contact types in graphene/Janus $MoGeSiN_4$ heterostructures, *J. Phys. Chem. Lett.* 12(16), 3934 (2021)
26. G. Kresse and J. Furthmüller, Efficient iterative schemes for *ab initio* total-energy calculations using a plane-wave basis set, *Phys. Rev. B* 54(16), 11169 (1996)
27. B. Hammer, L. B. Hansen, and J. K. Nørskov, Improved adsorption energetics within density-functional theory using revised Perdew–Burke–Ernzerhof functionals, *Phys. Rev. B* 59(11), 7413 (1999)
28. J. P. Perdew, K. Burke, and M. Ernzerhof, Generalized gradient approximation made simple, *Phys. Rev. Lett.* 77(18), 3865 (1996)
29. W. Zhang, S. Chen, M. He, G. Zhu, W. Yang, Y. Tian, Z. Zhang, S. Zhang, F. Zhang, and Q. Wu, Enhanced photocatalytic properties of $Bi_4O_5Br_2$ by Mn doping: A first principles study, *Mater. Res. Express* 5(7), 075512 (2018)
30. L. Li, W. Wang, H. Liu, X. Liu, Q. Song, and S. Ren, First principles calculations of electronic band structure and optical properties of Cr-doped ZnO, *J. Phys. Chem. C* 113(19), 8460 (2009)
31. D. Ghosh, G. Periyasamy, and S. K. Pati, Transition metal embedded two-dimensional C_3N_4–graphene nanocomposite: A multifunctional material, *J. Phys. Chem. C* 118(28), 15487 (2014)
32. A. J. Samuels and J. D. Carey, Molecular doping and band-gap opening of bilayer graphene, *ACS Nano* 7(3), 2790 (2013)
33. J. Bekaert, E. Khestanova, D. G. Hopkinson, J. Birkbeck, N. Clark, M. Zhu, D. A. Bandurin, R. Gorbachev,

S. Fairclough, Y. Zou, M. Hamer, D. J. Terry, J. J. P. Peters, A. M. Sanchez, B. Partoens, S. J. Haigh, M. V. Milošević, and I. V. Grigorieva, Enhanced superconductivity in few-layer TaS_2 due to healing by oxygenation, *Nano Lett.* 20(5), 3808 (2020)

34. Z. Sun, J. Xu, N. Mwankemwa, W. Yang, X. Wu, Z. Yi, S. Chen, and W. Zhang, Alkali-metal(Li, Na, and K)-adsorbed $MoSi_2N_4$ monolayer: an investigation of its outstanding electronic, optical, and photocatalytic properties, *Commum. Theor. Phys.* 74(1), 015503 (2022)
35. J. Robertson, High dielectric constant oxides, *Eur. Phys. J. Appl. Phys.* 28(3), 265 (2004)
36. J. Wang, W. Zhang, Q. Wu, S. Gao, Y. Jin, Y. Xiao, and Y. Chen, The electronic and optical properties of Au decorated($10\bar{1}4$) dolomite surface: A first principles calculations, *Results Phys.* 21, 103827 (2021)
37. Z. Zhao, Z. Li, and Z. Zou, Electronic structure and optical properties of monoclinic clinobisvanite $BiVO_4$, *Phys. Chem. Chem. Phys.* 13(10), 4746 (2011)
38. W. Yu, D. Xu, and T. Peng, Enhanced photocatalytic activity of g-C_3N_4 for selective CO_2 reduction to CH_3OH via facile coupling of ZnO: A direct Z-scheme mechanism, *J. Mater. Chem. A* 3(39), 19936 (2015)
39. L. Thulin and J. Guerra, Calculations of strain-modified anatase TiO_2 band structures, *Phys. Rev. B* 77(19), 195112 (2008)
40. A. Kudo and Y. Miseki, Heterogeneous photocatalyst materials for water splitting, *Chem. Soc. Rev.* 38(1), 253 (2009)
41. X. Li, P. Wang, Y. Wu, Z. Liu, Q. Zhang, T. Zhang, Z. Wang, Y. Liu, Z. Zheng, and B. Huang, $ZnGeP_2$: A near-infrared-activated photocatalyst for hydrogen production, *Front. Phys.* 15(2), 23604 (2020)
42. W. Zhang, Z. Zhang, S. Kwon, F. Zhang, B. Stephen, K. K. Kim, R. Jung, S. Kwon, K. B. Chung, and W. Yang, Photocatalytic improvement of Mn-adsorbed g-C_3N_4, *Appl. Catal. B* 206, 271 (2017)
43. J. Liu, Origin of high photocatalytic efficiency in monolayer g-C_3N_4/CdS heterostructure: A hybrid DFT study, *J. Phys. Chem. C* 119(51), 28417 (2015)
44. S. Chen, Y. Hu, S. Meng, and X. Fu, Study on the separation mechanisms of photogenerated electrons and holes for composite photocatalysts g-C_3N_4-WO_3, *Appl. Catal. B* 150–151, 564 (2014)
45. Z. Zhou, S. Yuan, and J. Wang, Theoretical progress on direct Z-scheme photocatalysis of two-dimensional heterostructures, *Front. Phys.* 16(4), 43203 (2021)